Int j simul model 21 (2022) 2, 296-307
Original scientific paper

EFFECTS OF FITTING ERROR ON THE HYDRAULIC PERFORMANCE OF BIONIC HYDROFOILS

Shi, H. X.; Meng, J.[#]; Li, Y.; Zhang, H. Z.; Wang, F. & Xu, W.
School of Mechanical Engineering, Hefei University of Technology, Hefei, 230009, China
E-Mail: jianm@mail.hfut.edu.cn ([#] Corresponding author)

Abstract
To improve the hydromechanical performance, sturgeon was chosen as the research object in this study, and a body surface structural model was built using 3D reverse engineering technology. An inhomogeneous B-spline curve fitting technique based on local refining was proposed. Meanwhile, three different bionic hydrofoils were designed and compared with three bionic hydrofoils gained from the least square method and NACA0015. Research results demonstrated that the new curve fitting technology can fit a high-accuracy hydrofoil (error $< 7\times10^{-4}$) by using only 15 control points, and the gained bionic hydrofoil has a good lift-drag ratio. With the bionic hydrofoils gained from the new curve fitting technology, the separation point of the laminar boundary layer moves toward the trailing edge of the hydrofoils, and the structure of the reflux eddy is refined. When two bionic hydrofoils were applied to the pump impeller structure, compared with NACA0015, the propulsive water-jet pump designed using the bionic hydrofoil gained from the new cutting fitting technology is in the scope of $0.8q_{th}$–$1.2q_{th}$, the head and efficiency are increased by about 7.05 % and 2.22 %, respectively.
(Received in March 2022, accepted in May 2022. This paper was with the authors 3 weeks for 1 revision.)

Key Words: Bionic Hydrofoil, B-Spline, Local Refinement, Transient Cavitation Flow

1. INTRODUCTION

Basic studies on the hydrodynamic properties of streaming around a hydrofoil have been the research hotspot in the academic circle [1, 2]. The geometric structure of a hydrofoil has important influences on the separation control of the streaming boundary layer, thus influencing the lift and drag properties of the hydrofoil. The blade section of hydraulic machinery is mainly composed of hydrofoil shape profiles, and the shape of the hydrofoil influences the hydraulic performance of the pump, turbine, and autonomic system (including autonomous underwater vehicle and underwater glider). Therefore, improving the distribution of streaming boundary layers of the hydrofoil and controlling the flow separation is of important significance to improve the lift and drag properties of the hydrofoil [3]. Traditional hydraulic machinery designed hydrofoils is mainly aviation airfoils based on aerodynamics, such as NACA and RAF airfoils. Nevertheless, the distribution of streaming boundary layers will be altered due to influences caused by the density and viscosity of the flowing medium, thus influencing the flow of the streaming fluid. Research and development of new hydrofoils and improvement of the hydraulic performance of hydraulic machinery have important significance to basic study on streaming around hydrofoils and studies on its adaptation to hydraulic machinery.

Fish accomplishes a series of basic behaviours by swimming, including foraging, avoiding risks, courtship behaviour, and migration [4]. Movement is a behavioural activity that consumes energy. When moving in water, fish can accelerate swimming quickly during foraging and make high-efficiency swimming during migration, in which the kinetic energy is transferred from body movement to fluid media to offset viscosity-related momentum and energy loss and acquire essential survival conditions at the minimum energy cost. Why can fish achieve the maximum benefits at the minimum energy cost? How do they overcome resistance? Reflections on these behaviours inspire practical engineering applications. Sturgeon, an aquatic vertebrate that can be dated back to the Cretaceous Period, has adapted to underwater life [5]. The body structure and appearance of sturgeon are different from those of other aquatic vertebrates. It can

jump out of the water to make courtship behaviours, capture preys in the air, or excrete parasites in high-altitude areas [6]. Such an ability of sturgeon demonstrates that the streamlined appearance, surface texture, and geometric shape of sturgeon can decrease resistance to some extent and minimize energy consumption by sending the body far away. The body surface has good hydraulic performance [7]. Sturgeon provides an element for the design of new bionic hydrofoils on the basis of hydrodynamics.

2. STATE OF THE ART

The hydrodynamics of a hydrofoil is influenced significantly by its shape, and even small changes may induce great influences [8]. Therefore, to decrease design error as much as possible and guarantee the comprehensive performance of new hydrofoils during design, an appropriate parameterization method should be applied to generate the desired geometric structure of hydrofoils. So far, common hydrofoil parameterization methods include the Hicks–Henne contour function method [9], PARSEC parameterization method [10], CST airfoil parameterization method [11], and spline parameterization method [12]. From a deep study, the parameterization design of an inhomogeneous B-spline curve has a better local control ability and fewer design variables compared with other methods. In B-spline curve fitting, the model curve can be gained through approximation of control points [13] and nodes [14]. Tai et al. [15] disturbed the control point of the curve by constrained optimization and discussed the problem in approximate combinations of two adjacent B-spline curves into one B-spline curve. Hu and Zhang [16] proposed a method to calculate the tangent vector of the corresponding data point in accordance with the geometric features reflected by the data point. Based on the constraint condition of the tangent vector (or preset) and control point, adaptive B-spline curve interpolation was carried out without preset nodes and control points by using the NSGA-II algorithm. Cheng et al. [17] proposed a new secondary B-spline curve and indicated that the traditional even B-spline curve/curve surface interpolation method may produce nonideal results. The problem lies in the selection of interpolation parameters rather than in the even B-spline curve and curve surface. The data points will influence the shape of the B-spline curve. Shen and Lin [18] proposed an adaptive cubic inhomogeneous B-spline curve interpolation algorithm. This algorithm adjusted the positions and quantity of points by using the large curve slope of the B-spline curve and further optimized the data points through the error between the B-spline curve and image edges. As a result, an algorithm should be developed in the engineering application field to decrease workloads and increase computational efficiency and applicability range while meeting the fidelity of the desired shape.

Inspired by specific biological functions, research scholars have applied these specific functions to engineering practices based on the bionic principle and achieved abundant research results. In accordance with the reflections on the swimming behaviours of long-body animals, Taylor [19] simulated their behaviours by using a cylinder and summarized relevant experimental data. He concluded that the body and swimming mode of fish have significant roles in advance. Nevertheless, the experimental results are not universal, and they are not applicable to conditions of high Reynolds number due to the excessive simplification on the swimming mode and shape of fish. Lighthill and Blake [20] proposed the slender body theory for fish swimming in the water and applied it to analyse the hydrodynamics of the movement mode of slender fish, which move by bending bodies. Fish et al. [21] acquired the geometric shape of the tail fin from samples of cetacean animals and gained the cross-section of samples by computer tomography based on X-ray. Later, he analysed the section, and the gained lift coefficient was 12 %–19 % higher than that of hydrofoils for engineering purposes. Based on the bionic concept, studies on various underwater propellers have been reported continuously, such as the robotic fish [22], and a dolphin-stroke bionic amphibious robot [23]. Aquatic

animals have very high manoeuvrability during swimming behaviours, and their body structure has an excellent performance in drag reduction and hydrodynamics.

To sum up, research scholars have conducted considerable studies on the construction of hydrofoil parameterization methods, optimal classical hydrofoils, acquisition of lift and drag properties, as well as the internal flowing characteristics of classical hydrofoils based on modern computational fluid-dynamic technology. Some research results have been achieved [24]. Nevertheless, exploration on the application of new bionic hydrofoils designed based on aquatic organisms (fish) to hydraulic machinery and improvement of the hydrodynamic mechanism of hydraulic machinery are rarely reported. In this study, sturgeon was used as the research object, and the body surface features were acquired in accordance with the geometric bionic principle. On this basis, a new hydrofoil parameterization method of three-time inhomogeneous B-spline based on local refinement was proposed. Meanwhile, a bionic hydrofoil geometric model with few control points, which can meet accuracy requirements, was constructed. Moreover, numerical simulation of different bionic hydrofoils based on large eddy simulation was carried out to acquire the lift and drag properties. The bionic hydrofoil was applied to axial-flow hydraulic machinery (a propulsive water-jet pump), and its advantages and disadvantages were compared. Relevant research results could provide hydrofoil references for the optimal design of hydraulic machinery blades.

The remainder of this study is organized as follows. Section 3 introduces the construction of the bionic hydrofoil model, the numerical computation method, and the grid independence test. Data fitting is implemented using a bionic hydrofoil and a NACA0015 airfoil, and the optimal fitting mode is chosen. Section 4 introduces the lift and drag coefficients and velocity fluctuation of the bionic hydrofoil and NACA0015 airfoil, as well as the verification of the practical application effect. Lastly, conclusions are presented in Section 5.

3. METHODOLOGY

3.1 Construction of the geometric model

Sturgeon is characterized by high response sensitivity and good surface streamline. It is a good bionic object to design bionic hydrofoils in this study. To avoid the influences of the individual differences of sturgeon on the general body surface characteristics, three types of sturgeon with different body sizes are selected as the research objects. A reverse modelling is implemented using a high-precision non-contact 3D scanner (accuracy = 0.02 mm), and the body surface characteristics are acquired (Figs. 1 a and b). The acquired point cloud data are input into the Geomagic Design X 3D reverse engineering software, and 3D geometric models of different sturgeons are constructed. The body surface characteristics of the same fish species meet geometric similarity; that is, the corresponding length–width ratio is the same. Finally, the average 3D geometric model of the sturgeon is gained through similarity conversion.

Given that the sturgeon is a 3D model, parameterization design of bionic hydrofoils has to be performed from different spatial scales to study the hydrodynamic properties of bionic hydrofoils based on the body surface characteristics of sturgeon comprehensively (Fig. 1 c). In this study, I (2/3h), II (1/3h), and III the horizontal plane where (0) locates are chosen as the reference planes (where h is the maximum thickness of the chord distance suction surface) to intersect with the 3D geometric models of sturgeons. In this way, three different original hydrofoil curves can be acquired. A coordinate system in Fig. 1 d is established using the fixed points of hydrofoils as the origin. The original hydrofoil curve is divided into several parts along the x-axis and marked by x_i (where $i = 0, 1, 2, \cdots, n$). The corresponding y-axis is expressed by $f_u(x_i)$. In this way, the original coordinate point (x_i, $f_u(x_i)$) on the original hydrofoil curve can be acquired, which can provide a data basis for the follow-up design of hydrofoils.

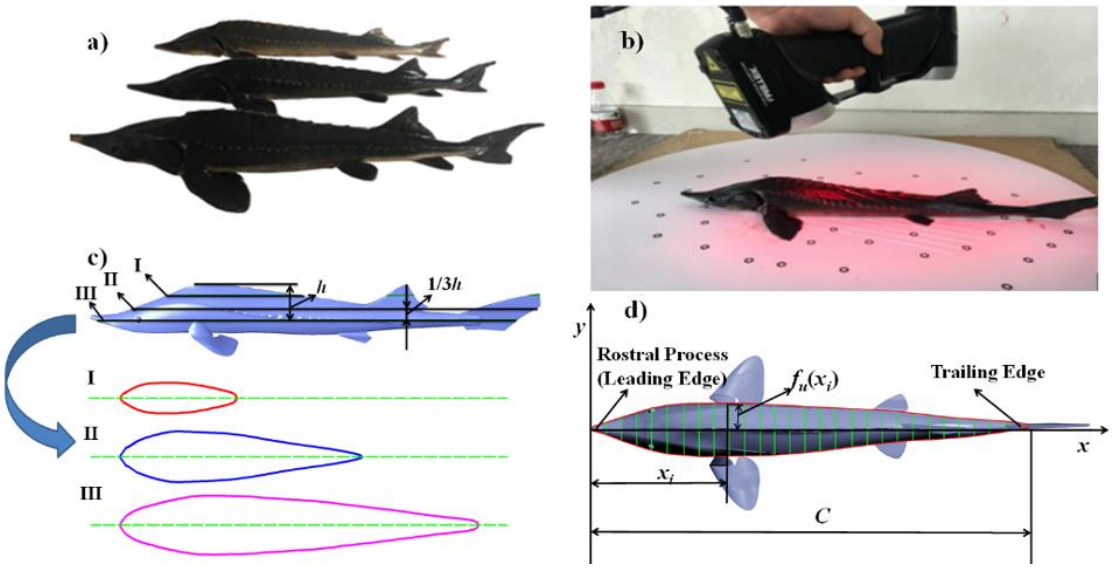

Figure 1: Acquisition of the profile curve of sturgeon body: a) three different sturgeons; b) physical scanning diagram; c) original hydrofoil curve; d) top view of sturgeon.

3.2 Hydrofoil parameterization design based on local refinement

The original coordinate points are gained from two common hydrofoil parameterization methods chosen for fitting, which are the curve fitting method based on the least square method and the segmented inhomogeneous B-spline curve fitting method. The advantages and disadvantages of these two methods are compared. Details are introduced in the following text.

Polynomial fitting:

The fitting equation is:

$$f_u(x_i) = c_m x^m + c_{m-1} x^{m-1} + \cdots + c_1 x + c_0 x^0 \tag{1}$$

where the coefficient (c_0, c_1, …, c_m) are calculated as:

$$\begin{bmatrix} n+1 & \sum_{i=0}^{n} x_i & \cdots & \sum_{i=0}^{n} x_i \\ \sum_{i=0}^{n} x_i & \sum_{i=0}^{n} x_i^2 & \cdots & \sum_{i=0}^{n} x_i^m \\ \vdots & \vdots & \ddots & \vdots \\ \sum_{i=0}^{n} x_i^m & \sum_{i=0}^{n} x_i^{m+1} & \cdots & \sum_{i=0}^{n} x_i^{2m} \end{bmatrix} \begin{bmatrix} c_0 \\ c_1 \\ \vdots \\ c_m \end{bmatrix} = \begin{bmatrix} \sum_{i=0}^{n} f_u(x_i) \\ \sum_{i=0}^{n} x_i f_u(x_i) \\ \vdots \\ \sum_{i=0}^{n} x_i^m f_u(x_i) \end{bmatrix} \tag{2}$$

where m is the highest number of terms of the polynomial, and it is determined as $m = 5$ in this study. The number of data points is n+1. The measured original coordinate point q_i is (x_i, $f_u(x_i)$) substituted into Eq. (2), so that the bionic hydrofoil design of the hydrofoil parameterization method can be realized. Three bionic hydrofoils were designed corresponding to the above three original hydrofoil curves, which were named P1, P2, and P3. Specifically, P1, P2, and P3 corresponded to the bionic hydrofoil cutting from profiles I, II, and III, respectively.

Segmented inhomogeneous B-spline fitting:

The equation of the piecewise inhomogeneous B-spline curve is:

$$B(u) = \sum_{i=0}^{n+2} B_i N_{i,k}(u) \tag{3}$$

where B_i (i = 0, 1, 2, ⋯, n + 2) are the control vertex and i represents the serial number. $N_{i,k}$ (i = 0, 1, 2, ⋯, n + 2) are the primary function of k standard B-splines, where k = 3. The primary function value is proposed using the Cox-de Boor formula.

$$N_{i,0}(u)=\begin{cases}1 & u\in[u_i,u_{i+1}]\\ 0 & u\notin[u_i,u_{i+1}]\end{cases} \tag{4}$$

$$N_{i,k}(u)=\frac{u-u_i}{u_{i+k}-u_i}N_{i,k-1}(u)+\frac{u_{i+k+1}-u}{u_{i+k+1}-u_{i+1}}N_{i+1,k-1}(u) \tag{5}$$

specifying zero for the quotient of 0/0 in Eqs. (4) and (5), and u_i refers to nodes. The definition domain of the curve is $u\in[u_k, u_{n+3}]$.

Calculation of nodes: Node vectors are acquired using the centripetal parameterization method (or called the root-squaring method). Data points at head and tail (q_0 and q_n) are used as the head and tail of the inhomogeneous B-spline interpolation curve. The internal data points (q_1, q_2, ⋯, q_{n-1}) are used as the segmented connecting points of the inhomogeneous B-spline interpolation curve, and the curve is divided into n sections. The control vertexes of the calculated B-spline interpolation curve are B_i (i = 0, 1, ⋯, n + 2), and the number of control vertexes is n + 3. The node vectors are U = [u_0, u_1, u_2, ⋯, u_{n+6}]. Hence, it is also called the segmented inhomogeneous B-spline curve fitting method. The specific node values are shown in Eqs. (6) and (7).

$$u_i=u_{i-1}+\sqrt{\Delta P_{i-3}}\quad(i=4,5,\cdots,n+2) \tag{6}$$

$$\Delta P_{i-3}=(x_{i-3}-x_{i-4})^2+(f_u(x_{i-3})-f_u(x_{i-4}))^2,\ i=4,5,\cdots,n+2 \tag{7}$$

The lead and tail of the curve are kept tangent with the leading edge (L.E.) and trailing edge (T.E.) of the control polygon. Thus, the multiplicity of lead and tail nodes is set to $k+1=4$; that is, $u_0=\cdots=u_3=0$ and $u_{n+3}=\cdots=u_{n+6}=1$. The original coordinate points q_1, q_2, q_3, ⋯, q_{n-1} are used as the segmented connecting points of the cubic B-spline interpolation curve, and the number of control points for calculation was $n+1$. To calculate all control vertexes, two additional equations must be added under the original conditions. In accordance with the calculated node vector and definition domain U = [u_0, u_1, u_2, ⋯, u_{n+6}], $u\in[u_k, u_{n+1}]$, the heavy node terms of the node vector are omitted, and the specific node values of the node vector [u_4, u_n] are substituted into the above B-spline interpolation equation. Therefore,

$$B(u_{i+3})=\sum_{j=i}^{i+2}B_jN_{j,3}(u_{i+3})=q_i,\ i=1,2,\cdots,n-1 \tag{8}$$

The number of Eq. (8) is $n-1$ and another four equations must be supplemented:

$$\begin{cases}B_0-B_1=\vec{0}\\ B_1=q_0\\ B_{n+1}=q_n\\ -B_{n+1}+B_{n+2}=\vec{0}\end{cases} \tag{9}$$

Combining with the solutions of Eqs. (8) and (9), the control vertex (B_i) is gained. Based on the Cox-de Boor recursion formula, the control point is substituted into Eq. (3), thus realizing bionic hydrofoil design based on the hydrofoil parameterization method. Three bionic hydrofoils are designed corresponding to the above three original hydrofoil curves, which are marked as B1, B2, and B3. Specifically, B1, B2, and B3 corresponded to the bionic hydrofoil cutting from profiles I, II, and III, respectively.

Segmental local refinement method:

Combining with Sections 3.2 (**Polynomial fitting**) and 3.2 (**Segmented inhomogeneous B-spline fitting**), the number of control points is the basis for the hydrofoil parameterization method. It is also the key to assuring the accuracy of the results of the constructed bionic hydrofoils. If enough original coordinate points (q_i) are acquired on the original hydrofoil curve in Section 2.1, the hydrofoil may approximate to the original hydrofoil curve infinitely.

Nevertheless, this will increase the workloads of researchers significantly, and its applications will be restricted. On this basis, a segmented local refinement method is proposed, which can decrease the number of control points to the maximum extent while assuring that the maximum fitting error is smaller than 7×10^{-4} in the allowable range [25]. The following text introduces this method based on NACA0015 and bionic hydrofoils B3.

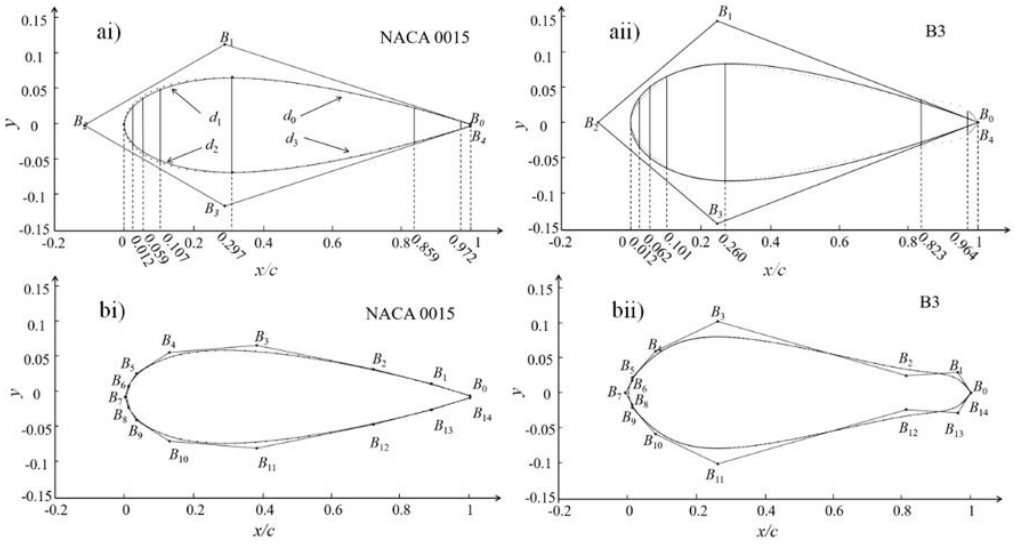

Figure 2: Curve fitting effects when the common ratio is 4: ai) before refinement of NACA0015; aii) before refinement of B3; bi) local refinement of NACA0015; bii) local refinement of B3.

The L.E. point ($x_i = 0$), the T.E. point ($x_i = 1$), and the maximum thickness points ($x_i = 0.297$ and $x_i = 0.26$) of hydrofoils were chosen as the boundary points to divide the hydrofoils into four sections, d_0, d_1, d_2, and d_3. Based on the boundary points, local refinements are performed at the L.E. and T.E. of bionic hydrofoils. The number of control points increased as the L.E. and T.E. are approached (Fig. 2). The difference between x-coordinates of two adjacent data points presented exponential functions, see Eq. (11). The refining process is carried out using an iterative computational method. If it finds that the maximum fitting error of a segment is higher than 7×10^{-4} during the hydrofoil parameterization process, it has to add a data point to this segment (coordinates of this data point are calculated by Eqs. (10) and (11)), thus increasing the control point (this control point was calculated using Eqs. (8) and (9)). Next, iterations are repeated until the maximum fitting error was smaller than 7×10^{-4}.

$$s_i = x_{i+1} - x_i / c \tag{10}$$

where s_i must be larger than and equal to 0.01. If $s_i < 0.01$, it is calculated in accordance with $s_i = 0.01$. $x_i + 1$ and x_i are the x-coordinates of two continuous control points. The common ratio (a) is defined as:

$$a = s_{i+1}/s_i \quad i = 0,1,2,\cdots,n-1,\ a \in (0,5] \tag{11}$$

The curve fitting effects when $a = 4$ of two hydrofoils (NACA0015 hydrofoil and B3 hydrofoils) before and after refinement are shown in Fig. 2. Figs. 2 ai and 2 aii depict that control points are distributed uniformly (before refinement). Under this circumstance, the maximum errors of the NACA0015 hydrofoil and B3 bionic hydrofoils after curve fitting are 0.01274 and 0.01369, respectively. Nevertheless, given the premise of the equal number of control points, the maximum errors of the two hydrofoils after curve fitting decreased significantly to 0.00066 and 0.00053 after local refinement technology. Moreover, they are both smaller than 7×10^{-4}, meeting the design requirements. To further explore the superiority of the local refinement technology, different values of a (1, 2, 3, 4, and 5) are set in this study. The relation between a and the number of control points is determined (Table I).

Table I presents that with the increase in a, the number of control points of the NACA0015 hydrofoil presented a V-shaped variation trend. The smallest number of control points is achieved when $a = 4$. Only 15 control points were needed to assure that the fitting error of curves is smaller than 7×10^{-4}. This scheme exerts the best fitting effect. Similar relations between a and the number of control points are observed in B3 bionic hydrofoils. The number of control points also decreased to 15 when $a = 4$. Likewise, it can meet the requirement that the error is smaller than the maximum allowable fitting error. Generally, if the fitting accuracy can be satisfied, B3 bionic hydrofoils are more beneficial for promotion and applications when the number of control points is smaller. When using classical NACA series hydrofoils, the number of control points is usually about 30 to assure the fitting accuracy [26]. The number of control points of the proposed segmented local refinement method could be decreased to 15 under the same fitting accuracy, indicating the significant superiority of the proposed method.

Table I: Comparison of schemes with different common ratios.

Hydrofoil	a	Number of nodes	Number of control points
NACA0015	1	29	23
	2	25	19
	3	27	21
	4	21	15
	5	29	23
B3	1	37	31
	2	31	25
	3	23	17
	4	21	15
	5	27	21

3.3 Physical and simulation setup

The computational domain (Fig. 3 a) is set by taking bionic hydrofoil B3 as example. The chord length (C) and angle of attack of the hydrofoil are 0.07 m and 6°, respectively. The dimension of the computational domain is 8C (length) × 3C (width). The inlet plane is at upstream 2.5C away from the hydrofoil centre, while the outlet plane is at downstream 5.5C away from the hydrofoil centre. The span width of the computational domain is 0.5C.

In this study, structured meshing is performed on the abovementioned computational domain by using the ICEM 19.2 software package. Grids in the computational domain are 3D grids (Fig. 3 b1). The 2D lateral view of the grids is shown in Fig. 3 b2. To capture details of unsteady flow, the peripheral regions of the hydrofoil are refined. The grid size near the surface of the hydrofoil along the flowing direction shall be smaller than or equal to 0.19 mm. Meanwhile, the grid size along the normal direction of the sidewall is smaller than or equal to 0.19 mm, and the grid size along the span direction is smaller than or equal to 0.2 mm. $y^+<1$. To verify the influences of grid quantity on the calculation results, grid independence is validated through a case study based on the B3 bionic hydrofoil. In this process, changes in lift coefficient (C_l) and drag coefficient (C_d) are compared (Table II). The lift and drag coefficients are defined as follows [27]: $C_l = F_l / 0.5\,\rho\, U_\infty^2\, A$ and $C_d = F_d / 0.5\,\rho\, U_\infty^2\, A$, F_l and F_d are the lift force and the drag force of the hydrofoil, respectively. A denotes the area projection of the hydrofoil. For the convenience of calculation, the area A is determined as the product of the chord length of the hydrofoil and the span. the flowing medium is 300 K water. The Reynolds number is $Re = \rho_m U_\infty C / \mu_m = 5 \times 10^5$, and the static pressure at the outlet is set by the number of cavitation: $\sigma = (p_\infty - p_v) / (0.5\,\rho_l U_\infty^2) = 0.65$, where p_v is the 25° saturated steam pressure, and the inlet velocity is $U_\infty = 7.2$ m/s.

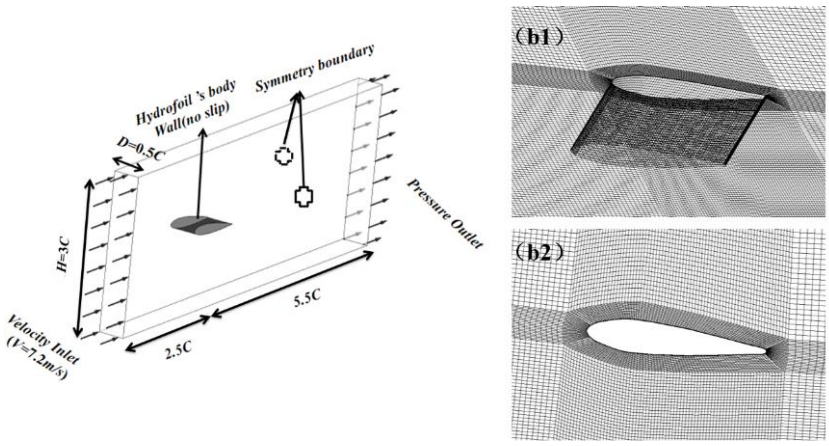

a) b)

Figure 3: Computational domain and meshing: a) 3D view of the computational region and boundary conditions, b) hydrofoil grid model, (b1) 3D grids, (b2) 2D grids.

In the verification of grid independence, five different grid sizes are chosen in the numerical calculation. The results are shown in Table II. When the grid quantity increased from Grid-1 to Grid-3, the C_l increased significantly, while the C_d decreased quickly. This result reflected that grid quantity could influence the test results greatly. When the grid quantity increased from Grid-3 to Grid-4, the C_l and C_d increased by 0.432 % and 0.926 %, respectively, smaller than 1 %. When the grid quantity increased from Grid-4 to Grid-5, the C_l and C_d are stable locally, and the growth hardly presented any changes. That is, after grid refinement, the C_l and C_d may fluctuate. Given enough grids, the C_l and C_d approached a constant. To decrease the requirements on the performance of computers, Grid-4 is chosen as the final meshing scheme. In other words, the grid quantity is about 4.1 million.

Table II: Verification of grid independence.

Grid	Number of cell	C_l		C_d	
Grid-1	1274064	0.441	---	0.111	---
Grid-2	1701103	0.454	2.948 %	0.109	1.802 %
Grid-3	2444064	0.465	2.423 %	0.108	0.917 %
Grid-4	4062528	0.465	0	0.107	0.926 %
Grid-5	5985480	0.466	0.215 %	0.108	0.935 %

4. SIMULATION ANALYSIS AND DISCUSSION

4.1 Lift-drag characteristics analysis

To verify the accuracy of the current numerical simulation method, numerical simulations of two groups of bionic hydrofoils (B1, B2, B3; P1, P2, P3) and the classical symmetric hydrofoil NACA0015 are carried out under the same boundary conditions. The mean values of the transient C_l and transient C_d of hydrofoils are calculated and compared. The results are listed in Table III. The results of the hydrofoil NACA0015, which is gained using the current research method, are compared with the experimental results in [27]. The average C_l and C_d of NACA0015 agreed with Ye's result, showing errors of 3.33 % and 1.83 %, respectively. The error of lift–drag ratio is 1.51 %. All of these errors are within the allowable reasonable range (<5 %). In a word, the current research method could disclose the lift and drag properties of bionic hydrofoils accurately, and it also can predict flowing laws in the flow field accurately.

Different data fitting schemes will produce various errors (the fitting error of hydrofoil P3 is 0.0067, the fitting error of hydrofoil B3 is 0.00053), hence different hydrofoil structures will

be obtained. This difference will eventually impact the lift-drag characteristics of the hydrofoil. Table III shows that bionic hydrofoils B3 and P3 are the optimal hydrofoils under B-spline and least square design schemes, respectively. Thus, the two hydrofoils are taken as examples.

Table III: Average lift-drag coefficient and lift-drag ratio for each hydrofoil.

Hydrofoil	**B1**	**P1**	**B2**	**P2**	**B3**	**P3**	**NACA0015**	
							LES	**Ye's result** [27]
C_l	0.439	0.402	0.434	0.433	0.460	0.445	0.465	0.481
C_d	0.116	0.113	0.113	0.116	0.101	0.109	0.107	0.109
C_l/C_d	3.783	3.558	3.841	3.741	4.554	4.083	4.346	4.413

4.2 Average velocity fluctuation

The streamline diagrams of NACA0015, B3, and P3 are shown in Fig. 4, which present the same laws and some differences. Such differences are caused by errors of design schemes. NACA0015, B3, and P3 have a common that velocity loss occurred near the surface of hydrofoils and the maximum fluid velocity is at the L.E. As the fluid particle moved gradually to the T.E. of the hydrofoil, the velocity declined gradually, accompanied by reflux. Finally, an eddy is formed on the suction surface of the hydrofoil. However, NACA0015, B3, and P3 also have some differences. The reflux velocity loss area of P3 is the largest, while the reflux velocity loss area of B3 is relatively smaller, and it is divided into two smaller ones. Moreover, the position of the reflux velocity loss zone moves significantly toward the T.E. compared with that in P3. Hence, the hydrofoil structural changes caused by the curve fitting error (the front curve of the hydrofoil shrank inward) might change the positions of the stream field around the hydrofoil and flow separation point.

The velocity distributions of B3, P3, and NACA0015 (on the upper surface of the hydrofoils, x/c = 0.2, 0.6, 0.8, 1.2) along the normal line of the sidewall are shown in Fig. 5. Comparison of the influences of geometric structures on velocity fields around hydrofoils indicated that the velocity field variations of bionic hydrofoils are similar to those of NACA0015. However, when fluid moves toward the T.E., the negative velocity growth of NACA0015 is close to the L.E., accompanied by the expansion of the sphere of influence of flows on the boundary layer and velocity variation range. This phenomenon could be explained in Fig. 4. From the comparison of the influences of curve fitting errors on the velocity fields of bionic hydrofoils, the velocity distributions on the near-wall surfaces of B3 and P3 differed significantly. Specifically, the velocity variation of B3 along the y-direction is relatively uniform, and it reaches the mainstream velocity earlier. Moreover, the location of negative velocity on the near-wall surface is closer to the T.E. In other words, curve fitting error would change the position of the separation point between the streamline layer and the boundary layer. The L.E. curve of the hydrofoil shrank inward to make the separation point closer to the L.E., thus expanding the reverse pressure range and increasing the resistance. Therefore, curve fitting errors must be considered during the design of hydrofoils.

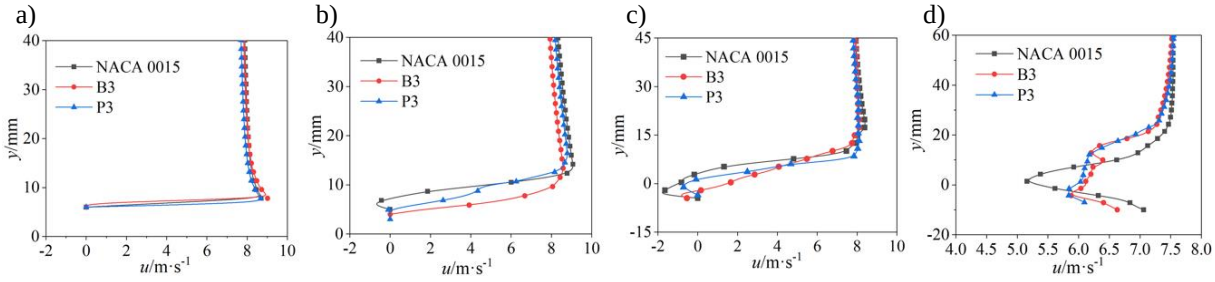

Figure 5: Distribution of average velocity (u) surrounding the hydrofoils along the y direction: a) x/c = 0.2, b) x/c = 0.6, c) x/c = 0.8, d) x/c = 1.2.

4.3 Application of bionic hydrofoil

To analyse the influences of curve fitting errors systematically, B3 and P3 are applied to thicken the blades of a propulsive water-jet pump [28]. It is compared with the original scheme (NACA0015 is used as the hydrofoil of the blade section). The other parameters are the same; however, the hydrofoil of impeller blades is changed, and the hydrodynamic curves in Fig. 6 are gained through numerical simulations, including the flow-head curve (H–q/q_{th}) and flow-efficiency curve (η–q/q_{th}). The running parameters of the propulsive water-jet pump are: $q_{th} = 456$ m³/s, $H = 4.0$ m, and rotating speed $n_w = 1600$ r/min. The geometric parameters of the impeller are as follows: outer diameter of impeller: $D = 200$ mm; hub diameter: $d_h = 80$ mm.

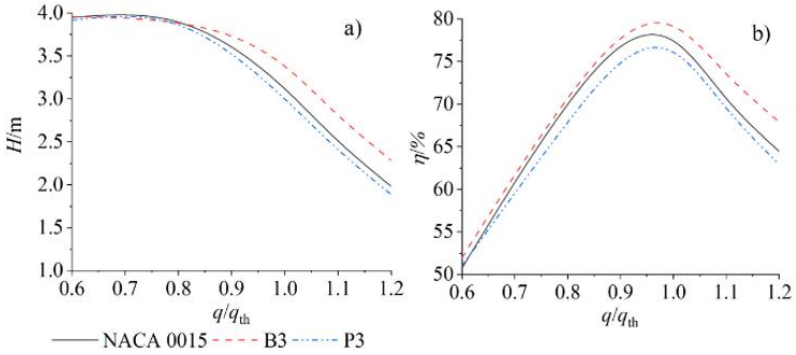

Figure 6: Hydrodynamic curves of the propulsive water-jet pump with different hydrofoil thickening blades; a) H–q/q_{th}; b) η–q/q_{th}.

Fig. 6 depicts that the head of the pump designed in accordance with B3 is the highest in the range of 0.8 q_{th}–1.2 q_{th}, whereas the head of the pump designed in accordance with P3 is the lowest. The corresponding efficiency curves show similar laws. This finding agrees with the abovementioned scheme (B3) with a greater lift-drag ratio completely. In other words, the higher the lift-drag ratio of the hydrofoil is, the better the performance of the pump would be. In view of the details, the designed operating points are compared. In Fig. 6 a, the head of the pump under the NACA0015 scheme ($H_{NACA0015} = 3.12$ m) is 7.05 % lower than that of the pump under the B3 scheme, but it is higher than that of the pump under the P3 scheme ($H_{P3} = 3.01$ m). Fig. 6 b shows that the pump designed in accordance with B3 has the highest efficiency ($\eta_{B3} = 79.13$ %), which is 2.22 % higher than that in the NACA0015 scheme ($\eta_{NACA0015} = 77.41$ %) and 4.0 % higher than that in the P3 scheme ($\eta_{P3} = 76.09$ %). Hence, bionic hydrofoils that use cubic inhomogeneous B-spline fitting can offer excellent hydrodynamic performance in terms of H-q/q_{th} or η-q/q_{th} when they are used for blade thickening of hydraulic machinery (propulsive water-jet pump).

5. CONCLUSION AND FUTURE WORK

In this study, basic data of sturgeon are acquired through 3D reverse engineering technology. Subsequently, the cubic inhomogeneous B-spline curve fitting technology based on local refinement is applied for the parameterization design of hydrofoils. The acquired bionic hydrofoils are applied to the blade design for a propulsive water-jet pump. The performance of the hydrofoils gained through the least square method and the propulsive water-jet pump is compared. The major conclusions are drawn as follows:

(1) Compared with a bionic hydrofoil obtained from the least square method, bionic hydrofoils gained from the cubic inhomogeneous B-spline curve fitting method based on local refinement can decrease the number of control points significantly while realizing satisfying accuracy. They only need 15 control points to assure curve fitting accuracy. This condition increases the possibility of extensive applications significantly.

(2) Geometric structural changes of hydrofoils may alter lift and drag properties, as well as flows in the near-wall boundary layer. Among all schemes, B3 can acquire better life and drag properties and a more stable flow in the boundary layer. From the comparison between B3 and P3, curve fitting errors may make the front curves of hydrofoils shrink inward, thus making the separation point move backward. Hence, a larger unstable reflux velocity loss region is formed after the separation.

(3) According to studies on the applications of bionic hydrofoils, a hydrofoil has a good lift-drag ratio, and the relevant propulsive water-jet pump also has good hydrodynamic performance. From the perspective of flow–head, and flow–efficiency curves, the pump designed in accordance with B3 shows higher head and efficiency in the range of $0.8\,q_{th}$–$1.2\,q_{th}$.

In this study, the hydrodynamic performance of the sturgeon hydrofoil is better than that of NACA0015. Research conclusions can provide important references for the optimization of the head and efficiency of fluid mechanical driving equipment. Nevertheless, this study only focuses on the performance of sturgeon hydrofoils under the same angle of attack. In the future, comparative analyses on the performance of hydrofoils under multiple angles of attack will be carried out by integrating particle image velocity measurement technology. They are conducive to the systematic analysis of the advantages of bionic hydrofoils.

REFERENCES

[1] Fernández-Gutiérrez, D.; van Rees, W. M. (2021). Effect of leading-edge curvature actuation on flapping fin performance, *Journal of Fluid Mechanics*, Vol. 921, Paper A22, 22 pages, doi:10.1017/jfm.2021.469

[2] Li, X.; Gu, J.; Su, Z.; Yao, Z. (2021). Hydrodynamic analysis of fish schools arranged in the vertical plane, *Physics of Fluids*, Vol. 33, No. 12, Paper 121905, doi:10.1063/5.0073728

[3] Liu, M.; Tan, L.; Cao, S. (2019). Dynamic mode decomposition of cavitating flow around ALE 15 hydrofoil, *Renewable Energy*, Vol. 139, 214-227, doi:10.1016/j.renene.2019.02.055

[4] Oufiero, C. E.; Whitlow, K. R. (2016). The evolution of phenotypic plasticity in fish swimming, *Current Zoology*, Vol. 62, No. 5, 475-488, doi:10.1093/cz/zow084

[5] Sulak, K. J.; Edwards, R. E.; Hill, G. W.; Randall, M. T. (2002). Why do sturgeons jump? Insights from acoustic investigations of the Gulf sturgeon in the Suwannee River, Florida, USA, *Journal of Applied Ichthyology*, Vol. 18, No. 4-6, 617-620, doi:10.1046/j.1439-0426.2002.00401.x

[6] Logan-Chesney, L. M.; Dadswell, M. J.; Karstern, R. H.; Wirgin, I.; Stokesbury, M. J. W. (2018). Atlantic sturgeon Acipenser oxyrinchus surfacing behaviour, *Journal of Fish Biology*, Vol. 92, No. 4, 929-943, doi:10.1111/jfb.13552

[7] Yan, H.; Yu, C.; Chai, L. P.; Li, Y.; Vnenkovskaia, V.; Chen, H. (2019). Design and investigation of the hydraulic performance of bionic hydrofoil based on the geometric features of sturgeons, *DYNA*, Vol. 94, No. 3, 278-285, doi:10.6036/9129

[8] Zhao, A.; Hui, Z.; Jin, H.; Wen, D. (2019). Analysis on the aerodynamic characteristics of a continuous whole variable camber airfoil, *Journal of Physics: Conference Series*, Vol. 1215, Paper 012005, 8 pages, doi:10.1088/1742-6596/1215/1/012005

[9] He, Y.; Sun, J.; Song, P.; Wang, X. (2021). Variable-fidelity hypervolume-based expected improvement criteria for multi-objective efficient global optimization of expensive functions, *Engineering with Computers*, Published online, 27 pages, doi:10.1007/s00366-021-01404-9

[10] Zhang, Y.; Wang, X. (2021). Global sensitivity and design space of drag characteristics of parametric airship hull, *Journal of Harbin Institute of Technology*, Vol. 53, No. 6, 54-61, doi:10.11918/201909018

[11] He, W.; Liu, X. (2019). Improved aerofoil parameterisation based on class/shape function transformation, *The Aeronautical Journal*, Vol. 123, No. 1261, 310-339, doi:10.1017/aer.2018.165

[12] Marinić-Kragić, I.; Vučina, D.; Ćurković, M. (2016). Efficient shape parameterization method for multidisciplinary global optimization and application to integrated ship hull shape optimization workflow, *Computer-Aided Design*, Vol. 80, 61-75, doi:10.1016/j.cad.2016.08.001

[13] Świta, R.; Suszyński, Z. (2018). Thermal image approximation using B-spline surfaces, *International Journal of Thermophysics*, Vol. 39, No. 11, Paper 127, 14 pages, doi:10.1007/s10765-018-2447-3
[14] Michel, D.; Zidna, A. (2021). A new deterministic heuristic knots placement for B-spline approximation, *Mathematics and Computers in Simulation*, Vol. 186, 91-102, doi:10.1016/j.matcom.2020.07.021
[15] Tai, C.-L.; Hu, S.-M.; Huang, Q.-X. (2003). Approximate merging of B-spline curves via knot adjustment and constrained optimization, *Computer-Aided Design*, Vol. 35, No. 10, 893-899, doi:10.1016/s0010-4485(02)00176-8
[16] Hu, L. C.; Zhang, W. S. (2020). NSGA-II approach for proper choice of nodes and knots in B-spline curve interpolation, *Computer-Aided Design*, Vol. 127, Paper 102885, 19 pages, doi:10.1016/j.cad.2020.102885
[17] Cheng, F.; Wang, X.; Barsky, B. A. (2001). Quadratic B-spline curve interpolation, *Computers & Mathematics with Applications*, Vol. 41, No. 1-2, 39-50, doi:10.1016/s0898-1221(01)85004-5
[18] Shen, H.; Lin, Y. (2016). Algorithm of B spline curve to describe image boundary, *Computer Engineering and Applications*, Vol. 52, No. 3, 174-177, doi:10.3778/j.issn.1002-8331.1403-0036
[19] Taylor, G. I. (1952). Analysis of the swimming of long and narrow animals, *Proceedings of the Royal Society A: Mathematical, Physical and Engineering Sciences*, Vol. 214, No. 1117, 158-183, doi:10.1098/rspa.1952.0159
[20] Lighthill, J.; Blake, R. (1990). Biofluiddynamics of balistiform and gymnotiform locomotion. Part 1. Biological background, and analysis by elongated-body theory, *Journal of Fluid Mechanics*, Vol. 212, 183-207, doi:10.1017/s0022112090001926
[21] Fish, F. E.; Beneski, J. T.; Ketten, D. R. (2007). Examination of the three-dimensional geometry of cetacean flukes using computed tomography scans: hydrodynamic implications, *The Anatomical Record: Advances in Integrative Anatomy and Evolutionary Biology*, Vol. 290, No. 6, 614-623, doi:10.1002/ar.20546
[22] Li, Q.; Zhang, J.; Hong, J.; Hu, D.; Yang, Y.; Guo, S. (2021). A novel undulatory propulsion strategy for underwater robots, *Journal of Bionic Engineering*, Vol. 18, No. 4. 812-823, doi:10.1007/s42235-021-0057-4
[23] Ding, R.; Yu, J.; Yang, Q.; Tan, M.; Zhang, J. (2011). Dolphin-like swimming modeling for a biomimetic amphibious robot, *IFAC Proceedings Volumes*, Vol. 44, No. 1, 9367-9372, doi:10.3182/20110828-6-IT-1002.01292
[24] Mao, L.; Wang, H.; Li, Y.; Yi, H. (2019). Force model of flapping foil stabilizers based on CFD parameterization, *Ocean Engineering*, Vol. 187, Paper 106151, 10 pages, doi:10.1016/j.oceaneng.2019.106151
[25] Sripawadkul, V.; Padulo, M.; Guenov, M. (2010). A comparison of airfoil shape parameterization techniques for early design optimization, *Proceedings of the 13th AIAA/ISSMO Multidisciplinary Analysis Optimization Conference*, Paper AIAA 2010-9050, 9 pages, doi:10.2514/6.2010-9050
[26] Zhang, D. H.; Xi, S.; Tian, D. (2014). Geometry control ability evaluation of classical airfoil parametric methods, *Advances in Aeronautical Science and Engineering*, Vol. 5, No. 3, 281-288, doi:10.3969/j.issn.1674-8190.2014.03.003
[27] Ye, W.; Yi, Y.; Luo, X. (2020). Numerical modeling of unsteady cavitating flow over a hydrofoil with consideration of surface curvature, *Ocean Engineering*, Vol. 205, Paper 107305, 10 pages, doi:10.1016/j.oceaneng.2020.107305
[28] Yan, H.; Li, Q.; Zhang, Y.; Shi, H. X.; Vnenkovskaia, V. (2018). Optimization of cavitating flow characteristics on RBSS of waterjet pumps, *International Journal of Simulation Modelling*, Vol. 17, No. 2, 271-283, doi:10.2507/IJSIMM17(2)427